Chapter 8

Ampere Class Energy-Recovery SRF Cavities

8.1 Introduction

Superconducting energy recovery linacs (SERLs) are increasingly becoming an attractive option for light sources, X-FELs, electron coolers and electron-ion colliders. SERLs show a potential to accelerate high current electron beams with high average current and brightness with ultra short bunches. The major challenge to accelerate high current beams is to overcome the dissipation of large amounts beam power into cavity modes making CW operation prohibitive. Fig. 8.1 shows a plot of average beam power deposited into an accelerating structure for some existing and future SERLs. The diagonal lines show contours of power normalized to a loss factor of 1 V/pC which is independent of accelerating structure used in the linac.

A five-cell superconducting cavity is under fabrication as a fundamental unit of the linac structure to accelerate the electron beam from 2.5 MeV to 54 MeV. This chapter focuses on the design and development of the first multicell cavity optimized for very high currents in an energy-recovery mode. HOMs excited by the beam can result in both single bunch (short range wakefields) and multi-bunch effects (long range wakefields) limiting the maximum charge per bunch and maximum current due to collective instabilities. The cavity design is optimized to suppress the effects of HOMs and increase the threshold currents beyond the ampere level. HOMs are studied in great detail to investigate their effects on the beam and the feasibility of accelerating high bunch charge ($>$ 20 nC) and high current ($>$ 1 A) beams. Measurements from a copper prototype of monopole and dipole modes are compared to simulations from numerical codes which show good agreement. Other important issues for superconducting cavities such as fundamental power coupler, multipacting, bellows shielding and Lorentz force detuning are also discussed.

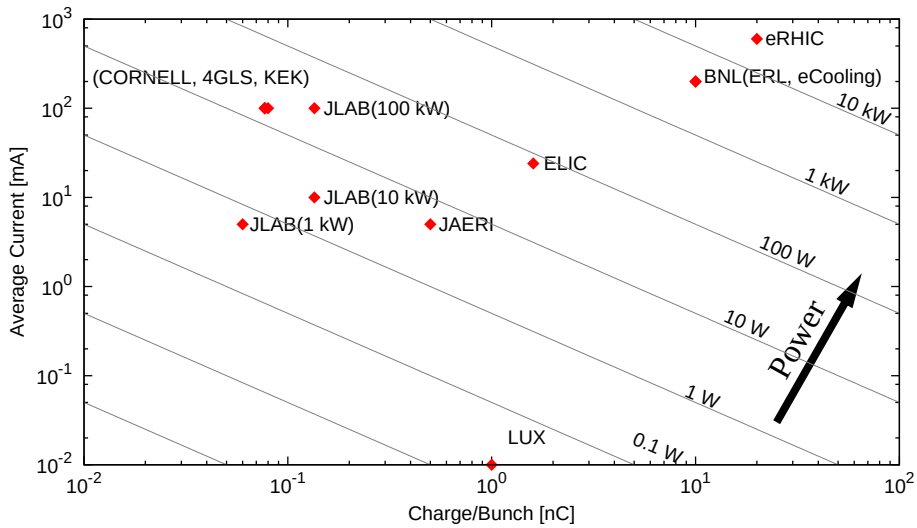

Figure 8.1: Average power dissipated due to single bunch losses in accelerating structures for exisiting and future SERLs. The diagonal lines represent the power contours normalized to a loss factor of 1 V/pC. Therefore, the power dissipated by the SERL facilities shown should be scaled to the actual loss factor of the accelerating structure used.

8.2 Cavity Design

The cavity design is greatly influenced by the operational modes of the linac. Several factors influenced the choice of key parameters of the cavity for high current energy recovery operation.

8.2.1 Frequency

A frequency choice of 703.75 MHz was made due to both physics and engineering issues. The precise frequency is the 25th harmonic of the RHIC bunch repetition frequency with 360 bunches. The power dissipated on cavity walls due to surface magnetic fields of the fundamental mode is proportional to

$$P \propto \frac{R_s}{\left(\frac{R}{Q}\right) G} \tag{8.1}$$

The surface resistance, $R_s = R_{BCS} + R_{res}$, where R_{BCS} is the BCS resistance of the superconductor ($\propto \omega^{1.8}$) and R_{res} is the residual resistance which is generally determined by the surface smoothness. Fig. 8.3 shows a plot of R_{BCS} as a function of temperature for three different frequencies that

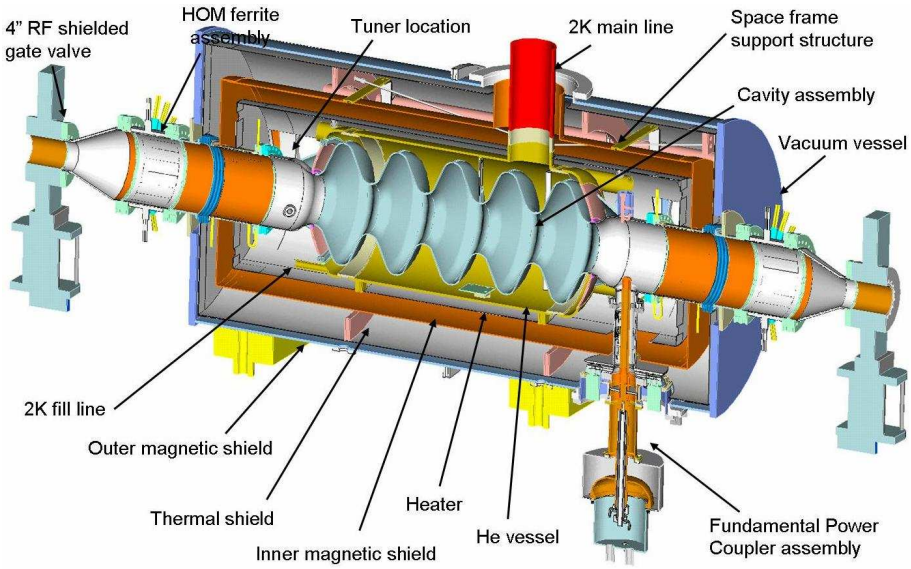

Figure 8.2: 3D cut away model of the five-cell cavity, cryostat, power coupler, ferrite absorbers, and feedthroughs (courtesy AES).

are widely used for superconducting linacs. If the R_{res} is sufficiently small ($\leq 1\ n\Omega$), a lower frequency significantly reduces cavity losses. If we assume that the cavity dimensions linearly scale with frequency, the factor $(R/Q)G$ is approximately constant for a constant number of cells, and therefore a lower frequency is preferable despite the increase in dimensions. However, the effective length of the linac decreases with increasing frequency which may help increase "real estate gradient" for long linacs.

A lower frequency allows a possibility of a large aperture resulting in a significant reduction of both longitudinal and transverse wakefields. This not only reduces HOM power deposited by the beam, but helps in raising the threshold current for the onset of multibunch instabilities in SERLs which are discussed in section 8.4 & 8.5. Availability of high power CW RF sources and compatibility with chemical cleaning facilities also played an important role to converge to 700 MHz region. A potential future use of this cavity in a linac-ring version of eRHIC was also considered.

8.2.2 Cavity Geometry

A parametrization developed in Ref. [68] for elliptical cavities to tune the shape for optimum electromagnetic and mechanical properties was used to design the cavity. The five-cell cavity is constructed from eight identical inner

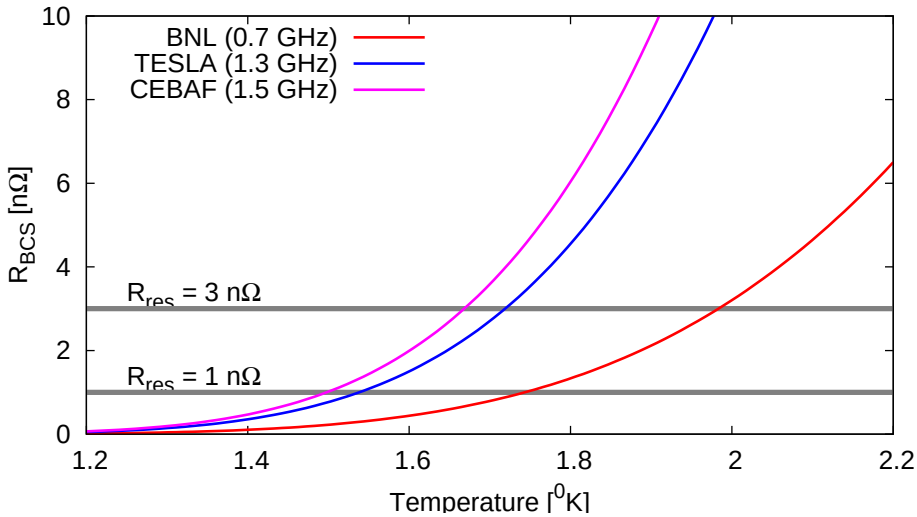

Figure 8.3: BCS surface resistance as a function of temperature for different operating frequencies. Here, the three frequencies correspond to the state-of-the-art SRF cavities being proposed or under operation in the energy recovery mode.

half cells and two end half cells. Each half cell can be described with the geometrical parameters shown in Fig. 8.4.

The geometrical parameters for the half cells were optimized using "Build Cavity", a graphics interface to Superfish [69]. The half-end cells are usually tuned separately for the freqency using the wall angle (α) or equator radius (D) to compensate for the beam tube. Several criteria like peak surface fields (E_{peak}/E_{acc}, B_{peak}/E_{acc}), shunt impedance (R/Q), cell-to-cell coupling (k_{cc}), and mechanical stiffness (dF/dR) were considered to optimize cell shape.

- Minimize peak surface fields, E_{peak}/E_{acc}, to avoid field emission at lower gradients and B_{peak}/E_{acc} to reduce surface losses or reach the magnetic breakdown limit. E_{peak}/E_{acc} is strongly dependent on the aspect ratio of iris ellipse (r), distance from cavity wall to iris plane (d), and iris radius (R_{iris}) as shown in Fig. 8.5(a), 8.5(b), and 8.5(c).

- A Large cell-to-cell coupling is important to avoid trapped HOMs especially in long structures. The coupling for the fundamental mode is mainly dependent on the iris radius (R_{iris}) as seen in Fig. 8.5(b), hence a large aperture is desirable. However, a larger iris does not always guarantee the best cell-to-cell coupling for all HOMs. Small irises should generally be avoided to reduce both the longitudinal and transverse loss

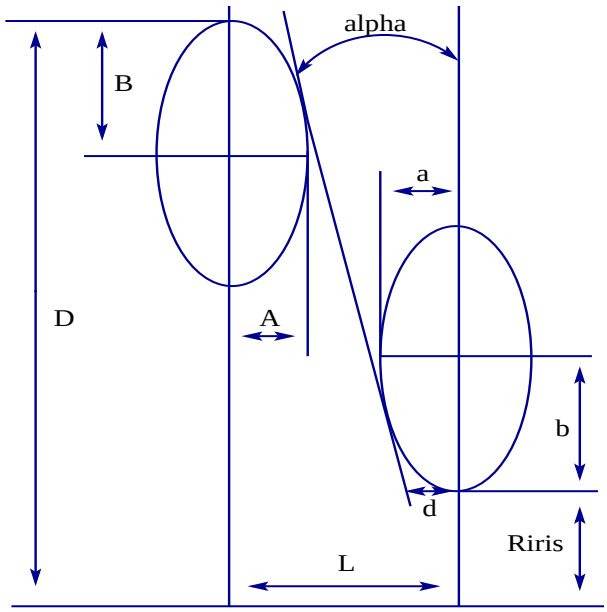

Figure 8.4: Parametrization of elliptical cavities.

factor. Other parameters like α, r, and d, were also optimized to maximize k_{cc}.

- Good mechanical stiffness to reduce the effects of microphonics and Lorentz force detuning while allowing a reasonable tuning capability. The equator aspect ratio (R_{eq}), α and d are dominating factors for mechanical stability. Larger α and d not only increase cavity stiffness but also helps in makes it easier for chemical treament of internal surfaces. However, larger wall angle also degrades k_{cc}, R/Q and H_{peak}/E_{acc} while improving E_{peak}/E_{acc} as seen Fig. 8.5(c).

- Minimize cavity wall losses by maximizing R/Q of the accelerating mode. R/Q decreases with a large aperture (Fig. 8.5 B), however extremely small surface resistance of SRF cavities allows one to significantly enlarge the aperture without much compromise. Therefore, HOMs are easily extracted through beam pipes even for multicell cavities.

The final optimized parameters describing the cavity geometry are listed in Table 9.4. An alternate design (BNL II) with modifications to α, d, and r is compared to the original design in Table 9.4. The main motivation for BNL II design was to reduce the cavity wall losses by increasing $\frac{R}{Q}G$. The cell-to-cell coupling and peak magnetic field were also improved at the cost of increasing

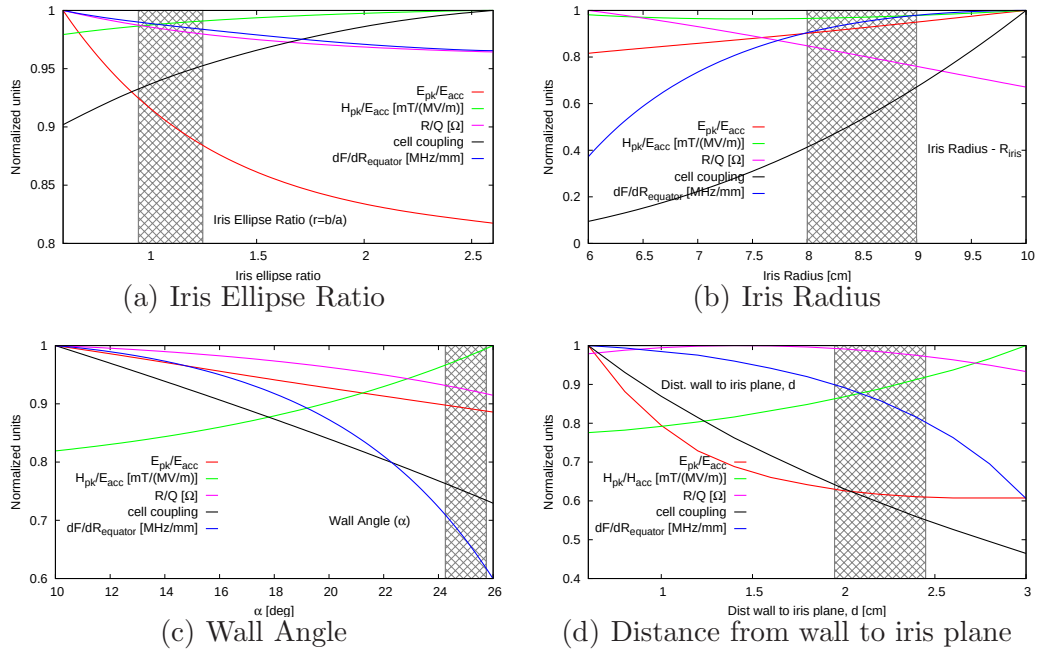

(a) Iris Ellipse Ratio (b) Iris Radius

(c) Wall Angle (d) Distance from wall to iris plane

Figure 8.5: Optimization of some relevant RF parameters as a function of each geomtrical tuning parameter. It should be noted that the tuning parameters are not completely independent of each other.

the peak electric field and reducing mechanical stiffness. Mechanical stiffners may become necessary to compensate the loss in stiffness for BNL II design. The inner half cell and half-end cell for BNL I & II are plotted in Fig. 8.6, and the relevant RF parameters are summarized in Table 8.2. A variant of BNL I design with the same middle cells and different end group is also shown in Fig. 8.6. The end group is tuned using the equator height (D) instead of the wall angle (α) unlike BNL I & II designs. Detailed analysis of these designs and some comparisons to the TESLA and CEBAF cavities are discussed in the follwing sections.

8.2.3 Number of Cells

Field flatness of the fundamental mode is an important factor to maximize the accelerating voltage and minimize surface fields for a given strored energy. A figure of merit that determines the acheivable field flatness for multicell

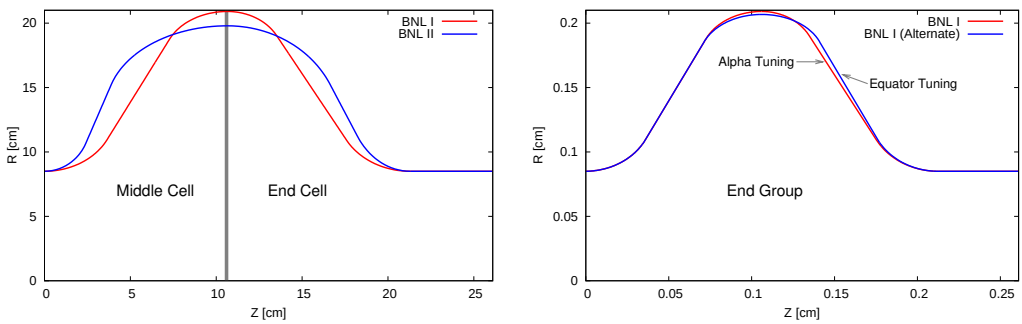

Figure 8.6: Final middle-cell and end-cell designs for five-cell cavity and an alternate design option, BNL II.

Table 8.1: Cavity geometrical parameters

Parameter	BNL I		BNL I-A	BNL II	
	Middle Cell	End Cell	Alt. End Group	Middle Cell	End Cell
Frequency [MHz]	703.75	703.75	703.75	703.75	703.75
Iris Radius, R_{iris} [cm]	8.5	8.5	8.5	8.5	8.5
Wall Angle, α [deg]	25	26.64	25	18	21.6
Equatorial Ellipse, $R = \frac{B}{A}$	1.0	1.1	1.0	0.9	1.2
Iris Ellipse, $r = \frac{b}{a}$	1.1	1.1	1.1	1.4	1.6
Dist. from cavity wall to iris plane, d [cm]	2.5	2.5	2.5	1.7	1.7
Half Cell Length, $L = \frac{\lambda\beta}{4}[cm]$	10.65	10.65	10.65	10.65	10.65
$H = D - (R_{iris} + b + B)[cm]$	4.195	4.160	3.792	1.254	-2.456
Cavity Beta, $\beta = \frac{v}{c}$	1.0	1.0	1.0	1.0	1.0

cavities can be expressed in terms of a field sensitivity factor given by

$$a = \frac{N^2}{\beta k_{cc}} \tag{8.2}$$

where N is the number of cells, $\beta = v/c$, and k is the cell-to-cell coupling. Larger a values limit the maximum achievable field flatness and make it more sensitive to mechanical tolerances. Table 8.2 shows a comparison of the field sensitivity factor for the BNL designs and are also compared to the TESLA and CEBAF cavity shapes.

Ampere class cavities require strong HOM damping ($Q_{ext} \leq 10^4$) due to large HOM power and multibunch effects that limit the maximum acheivable current. Since HOM extraction and damping in SRF cavities is constrained to the exterior of the structure, propagation of HOMs to the outside the cavity is imperative. Fig. 8.7 show an illustration of trapping an HOM in the interior cells as the number of cells is increased from 5 to 17. The increase in the number of cells gradually decreases the field in the end cells and beam pipe making it impracticle to extract and damp the HOM. Fewer cells with large

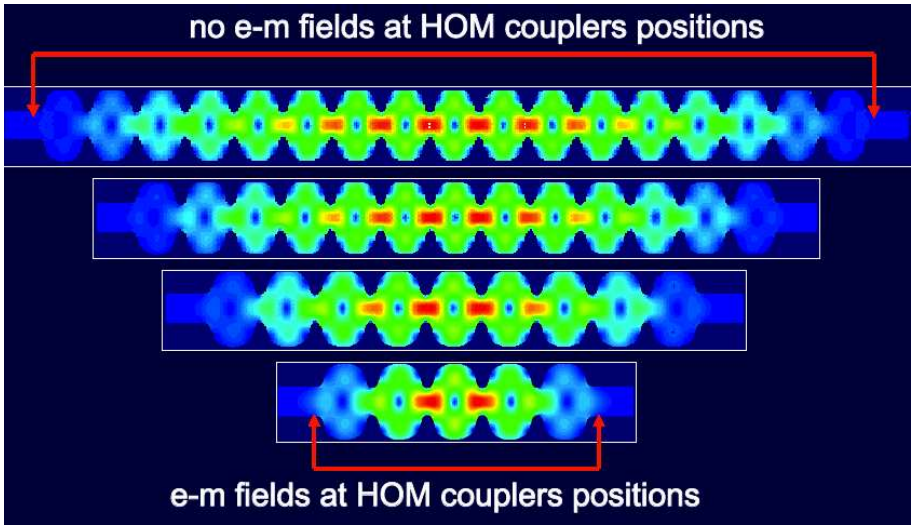

Figure 8.7: Effect of the number of cells on HOM propogation. Increase in number of cells causes the field of the HOM to be confined in the middle cells and makes it difficult to couple them out to a beam pipe load or HOM coupler.

k_{cc} not only improves field sensitivity factor for the fundamental mode but also help in achieve strong HOM damping. However, the active length of the linac is reduced. Therefore, five cells were chosen to be an optimum number to able to achieve effective damping while maintaining a reasonable accelerating gradient.

8.2.4 Beam Pipe Ferrite Absorbers

The beam pipe is a natural high pass filter and can be efficiently used to propagate HOMs to a load outside the cryogenic environment. Ferrite absorbers were the choice of HOM load because of their capability to absorb large HOM power and effective broadband damping with a simple and robust design. These absorbers are placed in the warm section (300 K) to minimize cryogenic losses.

Several highly lossy materials like C-48, Ferrite-50, and TT2-111V have proven to be excellent microwave absorbing materials (0.01-10 GHz) [72, 73]. A ferrite layer on a section of the beam pipe acts as a broadband HOM load. These absorbers have proven to be very successful in storage rings with single cell cavities (CESR & KEK-B). Fig. 8.8 shows a picture of ferrite assembly with "porcupine like" protrusions for water cooling [74, 75]. These absorbers have been tested upto 15 kW or higher and may become the only viable and

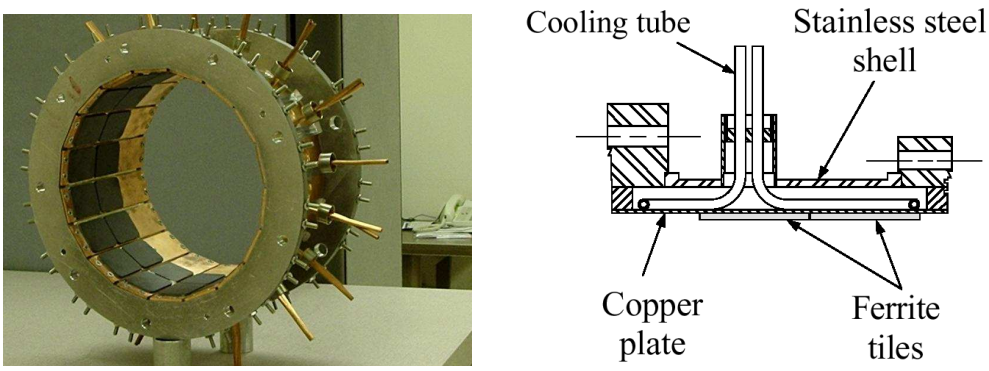

Figure 8.8: Ferrite absorber assembly [73]. The ferrite tiles are attached in copper plates provided with water cooling pipes. These plates are mounted on a stainless steel waveguide which is UHV compatible and assembled in class 100 clean room [74].

effective option for high power beams.

8.2.5 HOM Loop Couplers

A possibility of using TESLA type loop couplers for HOM damping was also considered in conjunction with the ferrite dampers. The loop couplers are required for TESLA type high "real-estate" gradient cavities with some HOMs that do not propagate along the beam pipe. They are placed very close to the cavity end-cell at superconducting temperatures to couple to the HOM fields in the end cell. However, they pose severe problems for high-current cavities due to extraction of large HOM power with a carefully tuned resonant circuit. Technical issues like the error in the notch frequency [76] and the temperature of the pick up probe [77] can lead to large cryogenic losses making it an undesirable candidate. Neverthless, a 3D model of the HOM loop coupler is designed for testing purposes in the five-cell cavity with the notch filter optimized for 703.75 MHz as shown in Fig. 8.9.

8.2.6 Beam Pipe Geometry

The damping of HOMs with ferrite absorbers require all mode frequencies above fundamental passband be sufficiently larger (> 20 MHz[1]) than cutoff

[1]The propagation (or attenuation) depends on the beam pipe length and diameter.

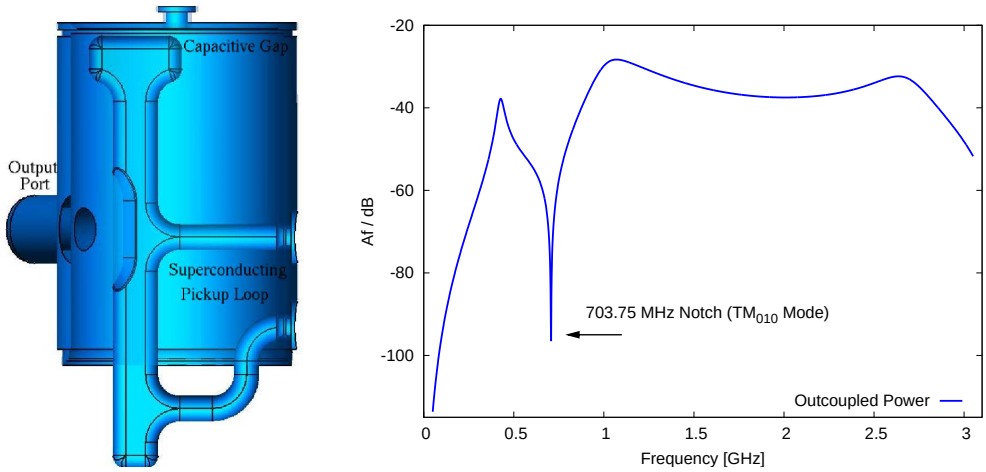

Figure 8.9: Cut away view of 3D model of the HOM loop coupler tuned for notch filter at 703.75 MHz (3D model courtesy AES).

frequency of the beam pipe. The cutoff frequency for a cylindrical waveguide is given by

$$f_c = \frac{c}{\pi D} X \tag{8.3}$$

where c is the speed of light, D is the diameter of the beam pipe, and X is the root of the Bessel function or its derivatives as appropriate. Fig. 8.10 shows plot of aperture size as a function of cutoff frequency for the first few monopole, dipole and quadrupole modes. For example, crossing of the vertical and horizontal line representing the frequency and beam pipe diamter is lower than the cut-off frequency line for TM_{011} implying that it is below cut-off. However, the crossing for TE_{111} is above the cut-off curve implying it is propagating into the beam pipe.

The beam pipe diameter was chosen such that the lowest monopole and dipole passband frequencies are well above their cutoff frequency. Fig. 8.11 shows a schematic of the end cell and beam pipe transition geometry. The transition consists of two elliptical sections of 5 cm each to gradually expand from a 17 cm iris to 24 cm beam pipe diameter. This enlargement causes an increase in the "leakage" of the fundamental mode field into the beam pipe, subsequently increasing cryogenic losses. A superconducting niobium transition is placed between cavity iris (2K) to the copper beam section ($\geq$ 5K) to minimize losses in normal conducting metals ($\leq$ 10 watts). A smooth transition of 10 cm from 17 cm to 24 cm aperture also reduces short range wakes from abrupt transitions. The cold to warm section of the beam pipe is equipped with a spiral channel for 5K helium gas flow to heat transfer the RF

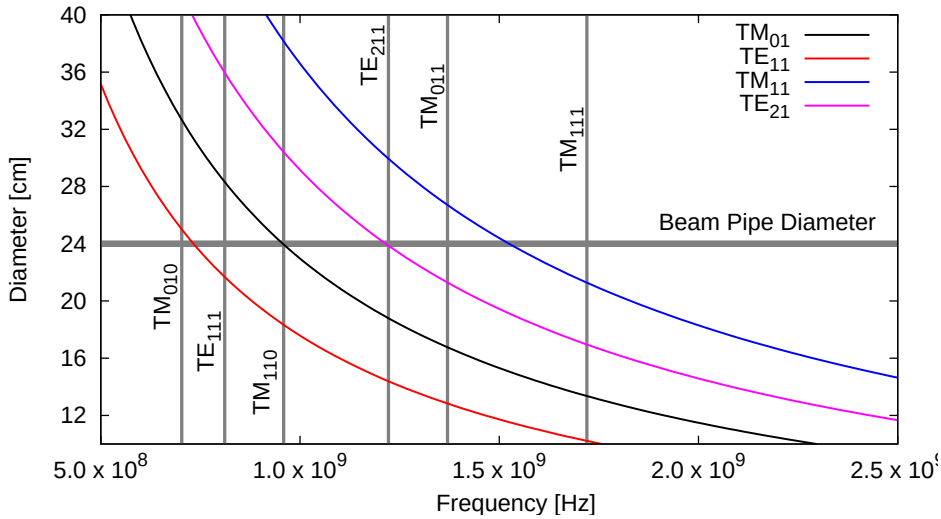

Figure 8.10: Cutoff frequencies of different types of modes in a cylindrical waveguide of a given diameter plotted as a function frequency. The vertical lines are frequencies of different modes for the five-cell cavity which may or maynot propogate depending on if they are above or below the cutoff.

losses in the beam pipe. Two sets of unshielded bellows (see Appendix D.3) are placed on the beam pipes to allow longitudinal and vertical motion during different phases of the cavity manufacturing and operation.

8.2.7 Final Design

A graphic of the final design of five-cell SRF cavity along with the coaxial fundamental power coupler (FPC) is shown in Fig. 8.12. Two full-size copper prototypes are manufactured to measure several properties of the cavity including field flatness, coupling, and most importantly HOM damping. Fig. 8.13 shows a comparison of calculated and measured field profile for the fundamental mode of the 5 cell cavity. The "moderatly" tuned copper prototype yields a field flatness of $96 \pm 1\%$ which agrees extremely well with electromagnetic (EM) codes giving 96.5%. The beam pipe enlargment causes additional leakage of the field resulting in a reduction in the field flatness. This reduction can be easily compensated by tuning the end cells. Some relevant RF parameters of the final design are listed in Table 8.2 and compared to BNL II, TESLA and CEBAF designs.

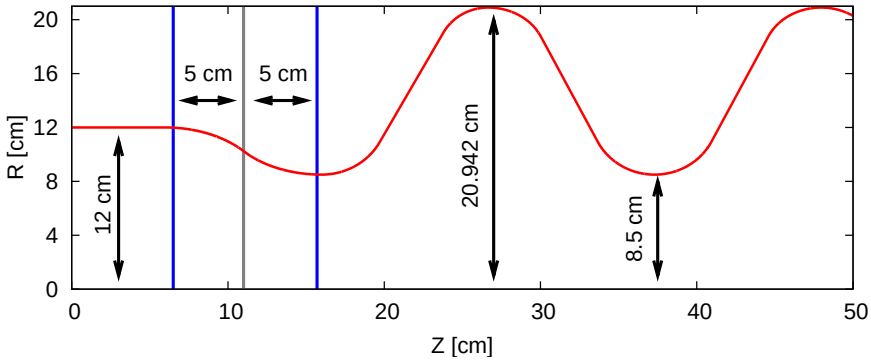

Figure 8.11: Beam pipe transition section consisting of two ellipses to transition from 17 cm iris diameter to a 24 cm beam pipe. The length of the transition section was determined to reduce the leakage of the fundamental into the beam pipe and also minimize the loss factor.

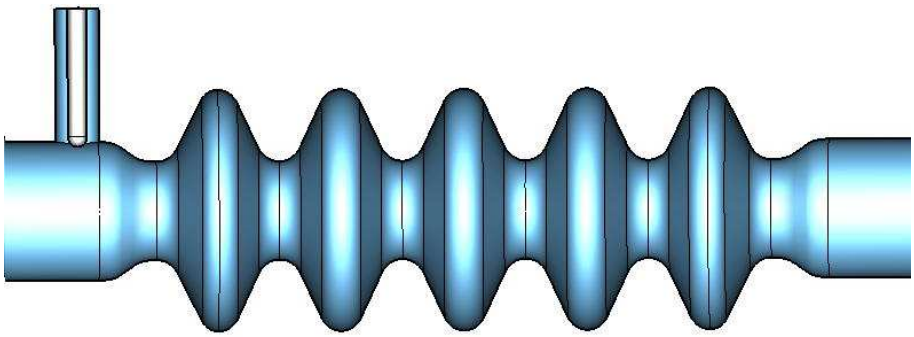

Figure 8.12: Graphic of the final design of the five-cell cavity, beam pipe transition and the coaxial FPC.

8.3 Higher Order Modes

The complex structure of multi-cell cavities can often lead to trapped modes which can be excited by the beam, leading to large HOM power and in some cases invoke beam instabilities. The three main causes of trapped modes are:

- Large number of cells trapping HOMs in the middle cells as discussed in section 8.2.3 and in Fig. 8.7.
- Small irises resulting in small cell-to-cell coupling thus trapping a mode. However, large irises can reduce R_a/Q_0 of the fundamental mode which is also undesirable (section 8.2.1).

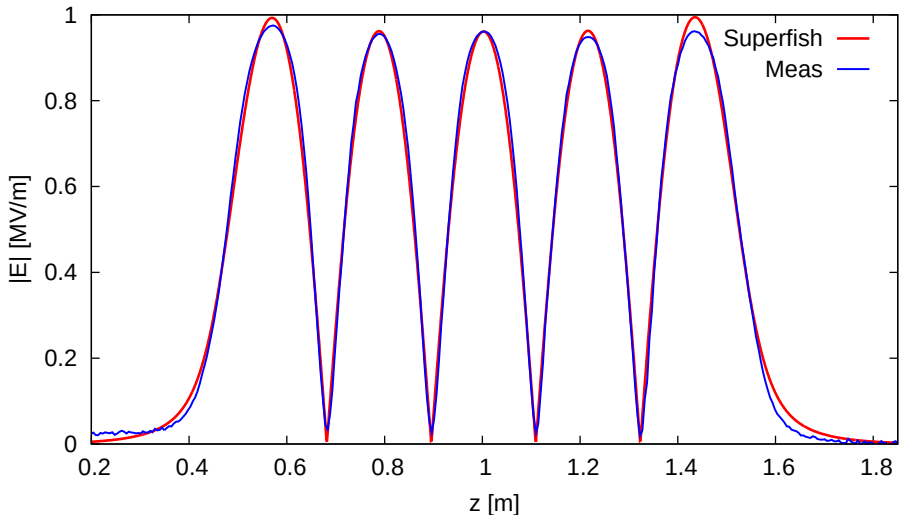

Figure 8.13: Field flatness of the fundamental mode peak-peak 96.5%.

- The presence of the beam pipe can result in an end cell geometry which significantly different from the middle cells. This can lead to a large deviation in the frequency of an HOM between the middle and the end cells. If this deviation is sufficiently large, the two cells are unable to resonate together thus trapping the mode. A simple example of an HOM in a TESLA cavity is compared to an HOM in BNL I cavity to illustrate the effect of a large frequency deviation.

- HOMs below the cut-off frequency of the beam pipe exponentially decay, and do not propagate into the beam pipe. The beam pipe diameter is enlarged to propagate all HOMs while staying sufficiently below the cutoff of the fundamental as illustrated in Fig. 8.10.

It is essential to study the behavior of HOMs and identify potentially trapped modes and damp them sufficiently. The following sections will focus primarily on the characteristics of monopole and dipole modes and their effects on the beam for the five-cell cavity. Comparisions to BNL II, TESLA, and CEBAF shapes are also made where appropriate.

8.3.1 Shunt Impedance and Quality Factor

Each HOM can be characterized by its shunt impedance R_a/Q_0 and a quality factor Q. R_a/Q_0 characterizes beam power deposited into a particular HOM excited by the beam. It is independent of the surface resistance of the

Table 8.2: RF Parameters for final design of BNL I cavity compared to an alternate BNL II, TESLA, and CEBAF cavities. NE - Not estimated.

Parameter	Unit	BNL 1(HC)	BNL 2 (HC)	CEBAF(HG)	TESLA(HG)
Frequency	[MHz]	703.75	703.75	1497	1300
Number of cells	-	5	5	7	9
$(R/Q) * G$	$[\Omega^2]$	9×10^4	9.58×10^4	2.1×10^5	2.8×10^5
E_p/E_a	-	1.97	2.25	1.96	1.98
H_p/E_a	$[mT/MV/m]$	5.78	4.88	4.15	4.15
Cell to cell coupling (k_{cc})	-	3%	4.45%	1.89%	1.87%
Sensitivity Factor ($\frac{N^2}{\beta k_{cc}}$)	-	8.3×10^2	5.6×10^2	2.6×10^3	4.1×10^3
Field Flatness	-	97.2%	97.3%	97.5%	95 %
Lorentz detuning coeff.	$[Hz/(MV/m)^2]$	1.28 (UnStiff)	NE	2	1

metals and is given by

$$\left(\frac{R}{Q}\right)_n = \begin{cases} \dfrac{|\int_0^d E_z e^{ik_n z} c dz|^2}{\omega_n U_n} & : \ monopole \ [\Omega] \\ \dfrac{|\int_0^d E_z(\rho{=}a) e^{ik_n z} c dz|^2}{(k_n a)^2 \omega_n U_n} & : \ dipole \ [\Omega] \end{cases} \tag{8.4}$$

where $k_n = \omega_n/c$ is the wave number of the mode with a frequency ω_n and stored energy U_n. Perturbation techinques can be used to measure R_a/Q_0, but numerical codes like MAFIA [78] are accurate and far less tedious. Fig. E.1 shows a computation of the $R/Q's$ for monopole and dipole modes upto 2.5 GHz. The R_a/Q_0 for just the fundamental mode is measured using the bead pull technique (see appendix D.1) using three different perturbing objects and results are compared to simulations in Table 8.3.

Table 8.3: Measurement of R_a/Q_0 using spherical beads. R/Q determined from MAFIA calculation is **403.5** Ω.

Material	R [mm]	R_a/Q_0 $[\Omega]$
Teflon	4.77 ± 0.02	474 ± 10
Steel	3.96 ± 0.01	532 ± 20
Aluminum	2.5 ± 0.01	370 ± 10

Microwave surface resistance of superconducting materials such as niobium are several orders of magnitude smaller than conventionally used copper. Therefore, the power dissipation in an SRF cavity wall is also small and can be

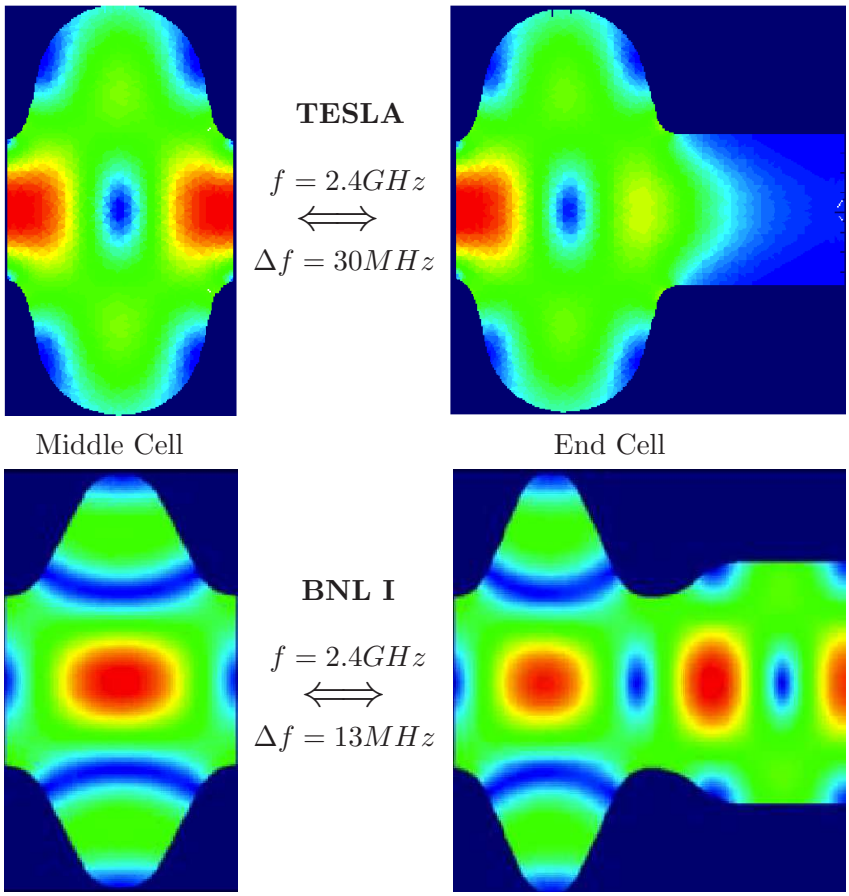

Figure 8.14: Illustration of trapped mode due to large difference in the frequency of the HOM between middle and end cell. The large difference prevents them from resonating together thus trapping the mode.

characterized by a high intrinsic quality factor, Q_0 given by Eq. 7.20. Typical Q_0 values of SRF cavities range anywhere between $10^9 - 10^{11}$. Since the power is dissipated partly in the cavity walls, and partly through beam pipe load, we define an effective Q_{tot} [2]

$$\frac{1}{Q_{tot}} = \frac{1}{Q_0} + \frac{1}{Q_{ext}} \tag{8.5}$$

For modes below the cutoff frequency the Q_{tot} is dominated by the cavity Q_0 (wall losses) and for modes propogating through the beam tube, Q_{ext} (load)

[2]Note that there is also power dissipated into the beam pipe walls and can be associated to Q_{ext} for modes below cut-off. For modes above cut-off, this can be neglected since the Q_{ext} is dominated by the external load.

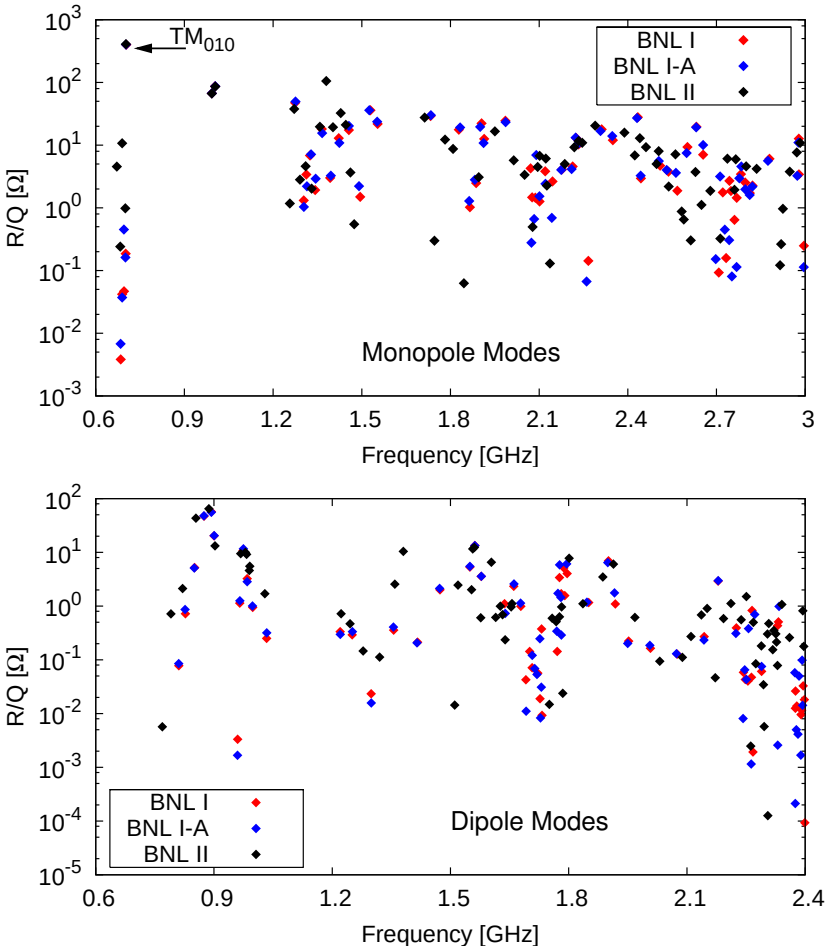

Figure 8.15: Shunt impedance (R/Q) calculated using MAFIA for monopole and dipole modes upto 2.5 GHz.

becomes the dominating factor. Numerical codes in frequecy and time domain are commonly used to estimate these high Q_0 factors of HOMs in superconducting cavities. However, numerical calculations are prone to errors and measurements can aid in benchmarking simulations. Boundary conditions play an important role in accurately determining HOM fields in a cavity and their propogation into beam pipe. Two different approaches will be discussed in detail and compared to measurements on a copper prototye.

8.3.2 HOMs: Frequency Domain

The conventional technique to identify possible trapped modes involves computation of the eigenmodes with two different boundary conditions at the beam tube termination [79]: electric wall or short-circuited transmission line ($\hat{n} \times \vec{E} = 0$) and magnetic wall or open-circuited transmission line ($\hat{n} \times \vec{H} = 0$). The influence of boundary conditions (BC) on the frequency can be used to infer the coupling of the mode to the beam pipe.

$$\kappa = 2\frac{|f_{mag} - f_{ele}|}{f_{mag} + f_{ele}} \tag{8.6}$$

$$\frac{1}{\kappa} \approx \begin{cases} 1 & : \ untrapped \\ \infty & : \ trapped \end{cases} \tag{8.7}$$

Fig. 8.16 shows a comparison of $\frac{1}{\kappa}$ as a function of frequency for the three designs for both monopole and dipole HOMs. For both longitudinal and transverse modes, BNL I and II show slightly different behavior but on average reveal coupling values of the same order of magnitude. For monopole modes, the $1/\kappa$ values are smaller than 10^3 with a majority of them below the 10^2 level. Therefore, we expect all the monopole HOMs to propogate through the beam pipe and be damped by the ferrite absorbers. Note that the fundamental mode is not shown in the plot since it is evanacent with $1/\kappa \approx \infty$. In the case of dipole modes, we see a few distinct bands with relatively higher values than the rest. BNL I show lower values for the 1st and 2nd passband, but have higher values for the $5^{th} - 7th$ pass band compared to BNL II design. It must be noted that lower frequency trapped modes are potentially more dangerous as the beam is more effective in exciting modes within its frequency spectrum ($\omega \sim \frac{1}{\sigma_z}$).

Another illustrative technique to study HOMs is to represent mode frequencies as a function of their phase advance per cell through dipersion curves. Although strictly valid for infinitely periodic structures, dispersion curves can also be calculated for finite structures by defining a corresponding function dependent on the longitunidal position to form a passband of modes. The slope of the dispersion curves represent the group velocity ($d\omega/dk$) of the passbands in an infinitely periodic structure. The dispersion curves can be calculated using numerical codes for a single cell with periodic boundary conditions

$$\hat{E}(r, z + L) = \hat{E}(r, z)e^{i\phi} \tag{8.8}$$

where $L = \lambda\beta/2$ is the cell length, and ϕ is the phase advance per cell. The dispersion curves for a periodic structure (BNL I) along with the dispersion

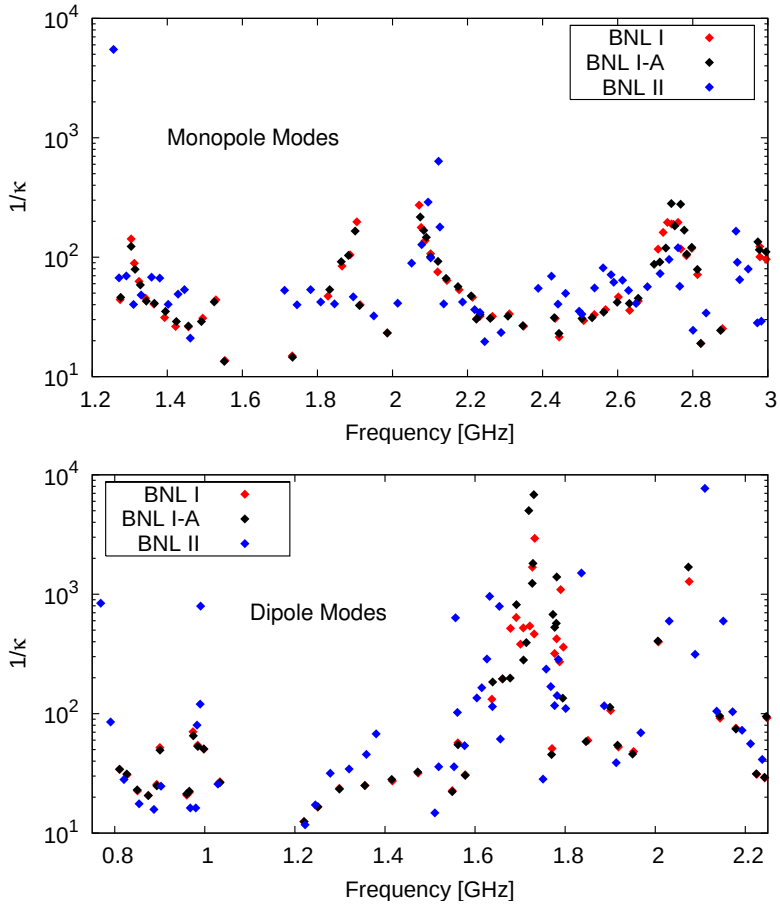

Figure 8.16: A coupling parameter κ shows the influence of the BC on the frequency of the mode. κ can be used identify possible trapped modes in the cavity.

curves for the five-cell cavity is shown in Fig. 8.17 for both monopole and dipole modes. The phase advance per cell for a finite number of cells can be determined from

$$\phi(z) = \arccos\left(\frac{E_z(r, z + L_{cell}) + E_z(r, z + L_{cell})}{2E_z(r, z)}\right). \tag{8.9}$$

The solid black line represents the light cone ($f_\phi = \frac{\phi c}{2\pi L}$) folded into the phase region between 0 to π.

The beam strongly excites modes that are synchronous to the beam, or simply modes with phase velocities equal to the speed of light ($v_\phi = c$). For monopole modes a select few in the $4^{th} - 8^{th}$ passbands are relatively close

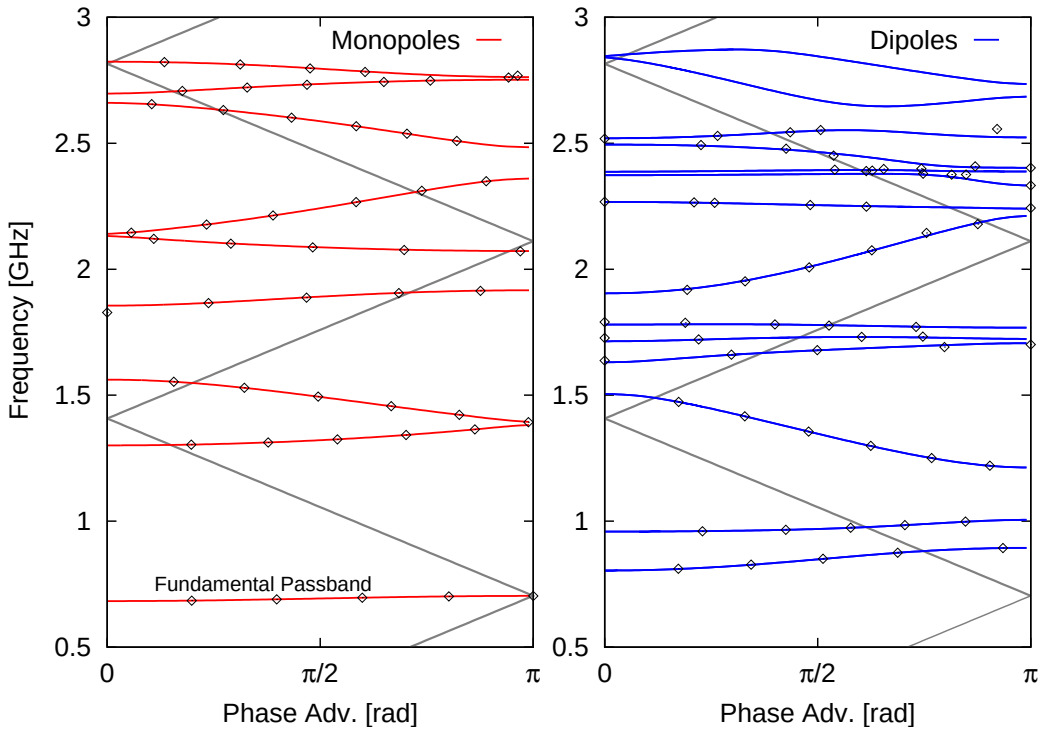

Figure 8.17: Dispersion curves of monopole and dipole modes for an infinite periodic structure along with the five-cell cavity (BNL I) for monopole (left) and dipole (right) modes. The black line is the light cone folded into the phase range from 0 to π.

to the light cone but none are exactly synchronous. It is interesting to note that successive passbands have alternating slopes and hence a symmetric beam pipe transition with ferrites on both sides of the cavity will be most effective in damping all higher order monopoles. In the dipole case, the 6th passband has a potentially synchronous mode with a frequency 1.78 GHz, and possibly some more modes above the 10th passband. A flat dispersion curve can make selective tuning of a single mode in the passband very difficult. This is particularly important for the fundamental passband where the accelerating modes is tuned continously to counteract Lorentz forces. The 5th and the 6th passbands have relatively flat dispersion curves, which may indicate to potentially trapped modes.

The most direct measure of a trapped HOM is to determine the external quality factor (Q_{ext}) of the mode which also ultimately sets the thresholds for the onset of beam instabilities. Numerical codes (like MAFIA) in frequency

domain formulated as a complex eigenvalue problem can be used to estimate $Q's$ of HOMs. The Q factor is given by [79, 78, 80].

$$Q_{ext} = \frac{1}{2}\frac{Re(f)}{Im(f)} \tag{8.10}$$

Since the damping is mainly due to beam pipe ferrites, it is important to include dissipative materials (complex ϵ and μ) in the simulation which are feasible in codes like MAFIA. However, highly dissipative materials like ferrites lead to long computational time and tend to cause the solutions to diverge or result in large errors. Therefore, calculations of Q_{ext} are restricted to small values of imaginary ϵ and μ (see Table 8.4). This approximation at worst should yield an upper limit to the Q_{ext} of HOMs. Although, numerical codes

Table 8.4: Lossy properties of ferrrite-50, C-48, and those used in MAFIA calculations. Note that values of the ϵ and mu are estimated from data in Refs. [73, 81]. The exact values are both both frequency and temperature dependent which are not taken into account in the calculation.

	C-48	Ferrite-50	MAFIA
ϵ_{Re}, ϵ_{Im}	(14.0, -1.5)	(12, -11.0)	(10.0, -1.0)
μ_{Re}, μ_{Im}	(2.0, -10.0)	(0.3, -1.0)	(2.0, -1.0)

have continually become better, it is customary to fabricate a copper prototype which is a useful tool to make several measurements and validate simulations. The prototype also aids as a learning tool in the fabrication process of complicated elliptical structures, and identify any pitfalls in the design of the cavity and its components. Fig. 8.18 shows the prototype of the five-cell cavity used to measure the Q_{ext} of HOMs upto 2.2 GHz. The cavity is placed in a tuning fixture which is used to tune individual cells for frequency and field flatness.

A comparison of simulations and measurments of Q_{ext} for modes upto 2.2 GHz is shown Fig. 8.19. In general the agreement between the simulations and measurements are quite good despite of the large difference in the lossy properties of ferrites in the simulations. The Q_{ext} for monopole modes are in the order of 10^3 or smaller. The agreement for dipole modes are exceptionally good, and in most cases the simulations show an upper limit as expected. The Q_{ext} values range between $10^2 - 10^4$ which are 2-3 orders of magnitude smaller than the currently state-of-the-art TESLA or CEBAF cavities. These small Q_{ext} values are needed to raise instability thresholds from milli-ampere to the ampere level and beyond. It must be noted that the measurements were done

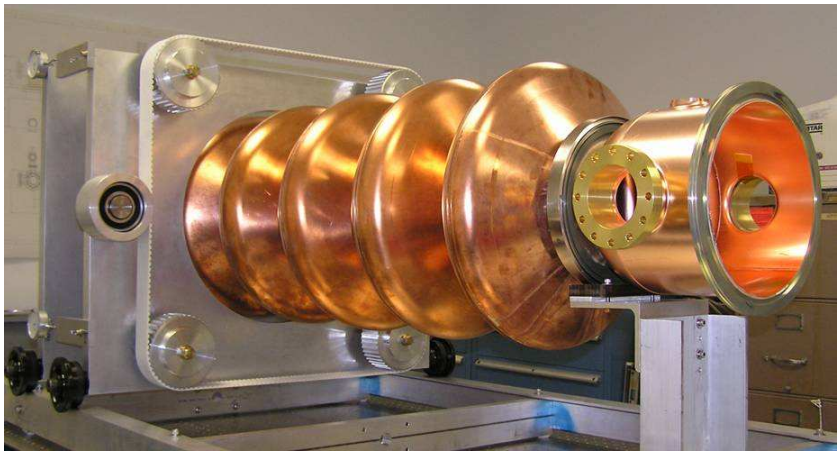

Figure 8.18: Full scale copper prototype used to measure Q_{ext} of HOMs the prototype ferrites (Fig. 8.8). The outer frame setup is the tuning fixture which will also be used to tune the final Nb cavity to 703.75 MHz.

using a single ferrite placed on either side and Q_{ext} was determined using

$$\frac{1}{Q_{ext}} = \frac{1}{Q_{left}} + \frac{1}{Q_{right}} \tag{8.11}$$

For modes with $Q_{L/R}$ in the noise level due to an asymmetric field distribution with respect to the cavity center, the Q from the side with the higher value was used as a pessimistic upper limit. Hence, a few measurements show larger values than the simulation, but in actuality are significantly smaller with symmetric ferrites on both ends.

More detailed simulations comparing an earlier geometry to BNL I design, and several numerical aspects such as mesh size, lossy properties of the ferrite, and comparison to other numerical codes were discussed in [111].

8.3.3 HOMs: Time Domain Method

In the frequency domain, one is limited to analyzing cavity modes with closed boundary conditions. This constrains one to rely on techniques described above to study HOMs and their effects. However, finite difference (or finite integration) time domain techniques allow one to simulate a real beam traversing any arbitary structure and the possibility of an infinite waveguide. The boundary is defined as perfectly matched layer with

$$\vec{\nabla} \times \vec{E} = -i\omega\mu\vec{H} - \sigma_M\vec{H} \tag{8.12}$$

$$\vec{\nabla} \times \vec{H} = -i\omega\epsilon\vec{E} - \sigma_E\vec{E} \tag{8.13}$$

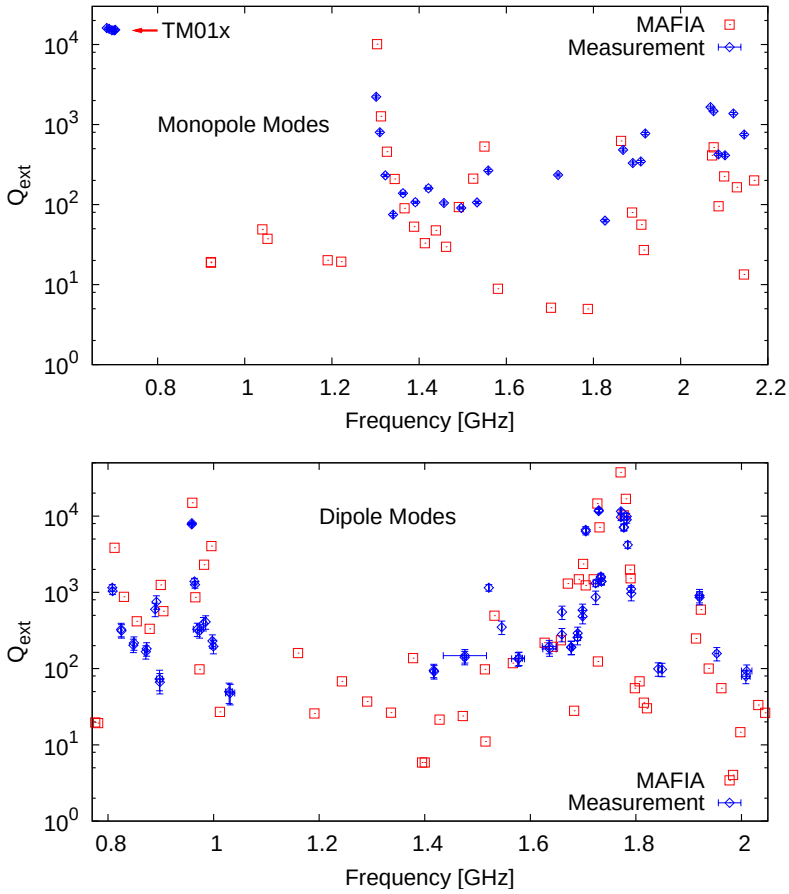

Figure 8.19: Top: Comparison of calculated and measured values of Q_{ext} for monopole modes (top) and dipole modes (bottom) upto 2.2 GHz.

where σ_E and σ_M are the electrical and magnetic conductivity and

$$(\vec{\epsilon}, \vec{\mu}) = (\epsilon_0, \mu_0) \left[\Lambda_{(\epsilon,\mu)} + \frac{\Sigma_{(E,M)}}{i\omega} \right] \tag{8.14}$$

are complex 3×3 matrices of permittivity, permeability and conductivity in the three dimensions [82]. These layers (or ports) allow waves above the cut-off frequency of the waveguide to propagate without any reflections at all incident angles. It is usually of interest to study the effect of the fields generated by a leading charge on a trailing particle which is commonly refered to as wakefields. The integrated effect of fields gives the longitudinal or transverse

wake potentials which are given by [83, 84]

$$W_{||}(\vec{r}, s) = -\frac{1}{q}\int_{-\infty}^{\infty}[E(\vec{r}, z, (s+z)/c)dz \tag{8.15}$$

$$W_{\perp}(\vec{r}, s) = \frac{1}{q}\int_{-\infty}^{\infty}[\vec{E}_{\perp} + c\ (\hat{e}\times\vec{B})]dz \tag{8.16}$$

The broadband impedance spectrum of the structure can be directly obtained from a Fourier transform of the wake potential normalized by the bunch spectrum $\rho(\omega)$ which is given by

$$Z_{||}(\omega) = \frac{1}{c\rho(\omega)}\int_{-\infty}^{\infty} W_{||}(\vec{r}, s)e^{-i\frac{\omega}{c}s}ds \tag{8.17}$$

$$Z_{\perp}(\omega) = -\frac{i}{c\rho(\omega)}\int_{-\infty}^{\infty} W_{\perp}(\vec{r}, s)e^{-i\frac{\omega}{c}s}ds \tag{8.18}$$

Since, the longitudinal and transverse wake potentials are related by the Panofsky-Wenzel theorem [85], the impedances are also related in the frequency domain as

$$\frac{\omega}{c}\ Z_{\perp}(\vec{r}, \omega) = \nabla_{\perp}\ Z_{||}(\vec{r}, \omega) \tag{8.19}$$

where $\nabla_{\perp} = \frac{\partial}{\partial r}\hat{r} + \frac{1}{r}\frac{\partial}{\partial\phi}\hat{\phi}$. In numerical codes like MAFIA, a Gaussian bunch with a charge density

$$\rho(s) = \frac{1}{\sqrt{2\pi}\sigma}e^{-\frac{(s-s_0)^2}{2\sigma^2}} \tag{8.20}$$

and length σ_z traveling at the speed of light can be launched in the cavity center or off-axis with appropriate boundary conditions to excite longitudinal (monopole like) or transverse (dipole like) modes respectively. MAFIA computes the longitudinal wake potential as a function of bunch coordinate (s = ct) which can then be Fourier transformed to calculate the impedance spectrum. Since, trapped HOMs in SRF cavities can have high Q factors, long-range wake potential computations are usually required to estimate the impedance accurately. If Q factors are extremely high, the spectrum of that mode is artificially broadened due to the truncation of the wake. In such cases the impedance can be better approximated using two different long-range computations [96]. To investigate high Q modes in the five-cell cavity, wake computations upto 300 m were performed. Fig. 8.20 shows broadband impedance spectrum of longitundinal modes compared to measurements performed on the copper prototype. It should be noted that the impedance measurements are a product of the shunt impedance of each individual mode with the measured external Q from

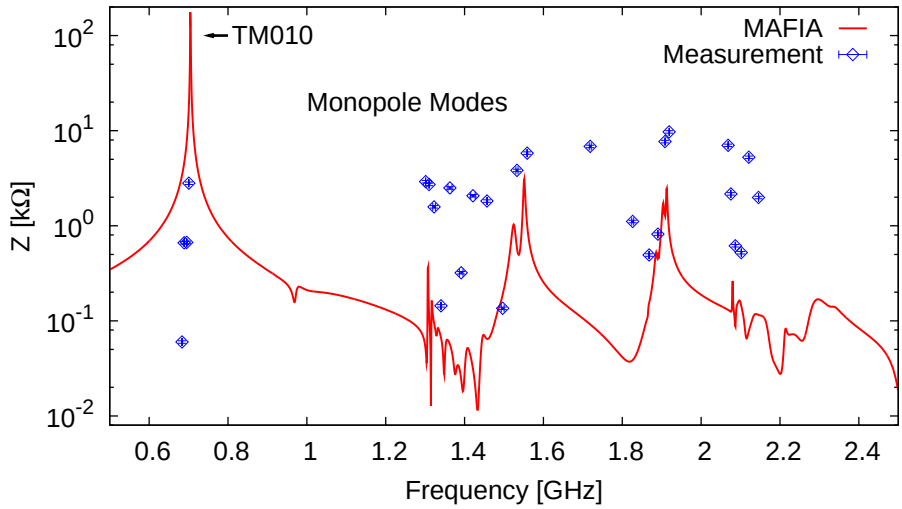

Figure 8.20: Impedance spectrum and wake function for azimuthally symmetric modes

the prototype and hence can be different from the beam coupling impedance as calculated using the wake potential. The spectrum is dominated by the fundamental mode as expected and all other monopole modes with rather small impedances. There is only partial agreement with simulation and measurements due to the measurement technique for modes in the noise level giving an upper limit as described in section 8.3.2. Neverthless, we do not find any high Q trapped monopole modes.

A similar calculation for transverse deflecting modes was performed by displacing the bunch by 3 cm from the cavity center with appropriate boundary conditions to selectively excite dipole modes. Fig. 8.21 shows impedance spectrum for the dipole modes compared to measurements performed using the prototype. The agreement for the relatively higher Q modes are very good. The spectrum shows two distinct bands of interest: 1st and 2nd passband in the 0.9 GHz region and $4^{th} - 6^{th}$ passband near the 1.7 GHz region similar to that of the frequency domain results. Both regions yield external Q factors smaller than the 10^4 and are sufficiently damped to suppress both single bunch and multibunch effects which are studied in the following sections.

8.4 Single Bunch Effects

A beam traversing a structure losses energy into the structure dominated by single bunch losses primarily from longitudinal modes. The power lost is

given by

$$\frac{dE}{dt} = \frac{c^2}{2\pi R} \int_{-\infty}^{\infty} |\rho(\omega)|^2 \; Z_{||}(\omega) d\omega \tag{8.21}$$

where R is the aperture radius, $\rho(\omega)$ is the bunch spectrum, and $Z_{||}$ is the longitudinal impedance. For a Gaussian bunch of RMS length σ_z, the power lost can be expressed as

$$P_{lost} = k_{||} q_b^2 f_b \tag{8.22}$$

where Q_b is the bunch charge, f_b is the beam repetition frequency, and $k_{||}$ is the longitudinal loss factor which is given by [86]

$$k_{||}(\sigma) = \frac{1}{2\pi} \int_{-\infty}^{\infty} Z_{||}(\omega) f(\omega, \sigma) d\omega \tag{8.23}$$

where $f(\omega, \sigma) \approx e^{-\omega^2 \sigma^2}$ is the spectral power density of a Gaussian bunch. For a cavity with discrete modes, the longitudinal loss factor for a given mode can be expressed as

$$k_{||}(n) = \frac{1}{2\pi} \int_{-\infty}^{\infty} Re Z_{||}(\omega) d\omega. \tag{8.24}$$

In the high Q regime and in the neighborhood of the resonance,

$$\mathrm{Re}(Z_{||}) = \frac{Z_n}{1 + [2Q(\omega - \omega_n)/\omega_n]^2}. \tag{8.25}$$

Therefore, the loss factor integral simplifies to

$$k_{||}(n) \approx \frac{\omega_n}{4} \left(\frac{R}{Q} \right)_n \tag{8.26}$$

where $(R/Q)_n$ is the accelerator physics definition of the shunt impedance of the nth mode. The longitudinal short range wake excited by the beam induces an energy spread in the beam which can be calculated using [86]

$$\frac{\delta E}{E} = \frac{2 Q_b k_{||}}{E_{acc}}. \tag{8.27}$$

Therefore, $k_{||}$ has to be minimized especially for high charge scenarios.

A beam off-axis can excite deflecting modes (dipole like) and generate transverse wakefields. These transverse wakefields in turn act back on the

beam and give an effective kick which can be characterized by analogous transverse loss factor given by [86]

$$k_{\perp}(\sigma) = \frac{1}{2\pi} \int_{-\infty}^{\infty} Z_{\perp}(\omega) f(\omega, \sigma) d\omega \tag{8.28}$$

where $Z_{\perp}$ is the transverse impedance of the structure. The transverse wake gives rise to kick thus displacing the tail with respect to the head and resulting in an emittance growth which can estimated from [63]

$$\frac{\Delta x}{x} = \frac{Q_b k_{\perp}}{2E_{acc}} \langle \beta \rangle \; ln \frac{\gamma_f}{\gamma_i} \tag{8.29}$$

where, E_{acc} is the accelerating gradient, $\langle \beta \rangle$ is the average beta function.

The loss factor for the five-cell cavity was calculated using ABCI [87], a numerical code for azimuthally symmetric structures. Fig. 8.22 shows the integrated loss factor as a function of frequency for a gaussian bunch of RMS length of 1 cm traveling through the cavity for BNL, TESLA and CEBAF deisgns. The integrated loss factors and the corresponding power dissipated for electron cooling scenario with 5 nC bunch charge and 50 mA beam current are listed in Table 8.5. The loss factors per single cell of the BNL, TESLA and CEBAF designs are plotted in Fig. 8.23 as a function of bunch length for comparison. For bunch lengths of 1 cm or smaller, the BNL design has clearly much smaller $k_{||}$ and $k_{\perp}$ and hence better suitable in high current high bunch charge regime. In addition the lower BNL's lower frequency allows the possibility of longer bunches. Estimates for the energy spread and the emittance growth induced by the corresponding accelerating structures are shown in Table 8.5 for nominal bunch length ($\sigma = 1\ cm$), bunch charge ($Q_b = 5\ nC$) and an energy gain of 20 MeV through the accelerating structure.

Table 8.5: Longitudinal and transverse loss factors for final design (BNL I). Loss factors for an alternate design (BNL II), TESLA and CEBAF cavities are also listed for comparion (σ_z = 1 cm, Q_b = 5 nC, and E_{gain} = 20 MeV). NE - Not Estimated

Parameter	Unit	BNL I (HC)	BNL II (HC)	CEBAF(HG)	TESLA(HG)
$k_{\|\|}$ (σ_z - 1 cm)	[V/pC]	1.07	1.18	2.84	3.56
$k_{\perp}$ (σ_z - 1 cm)	[V/pC/m]	3.19	3.37	48.84	45.71
$\delta E/E$ (Q - 5 nC)	-	0.05 %	0.06 %	0.14 %	0.18 %
$(\Delta\epsilon)/\epsilon_0$ (Q - 5 nC)	-	NE	NE	NE	NE

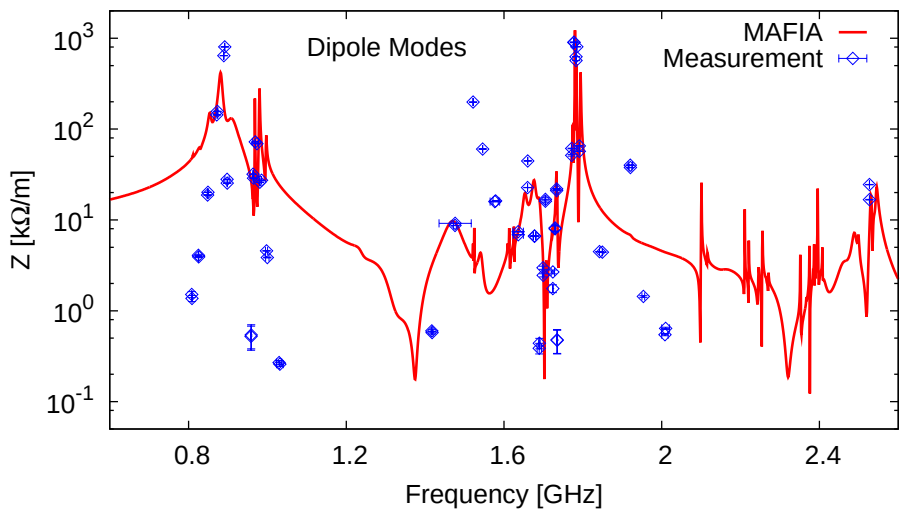

Figure 8.21: Impedance spectrum and wake function for transverse dipole modes

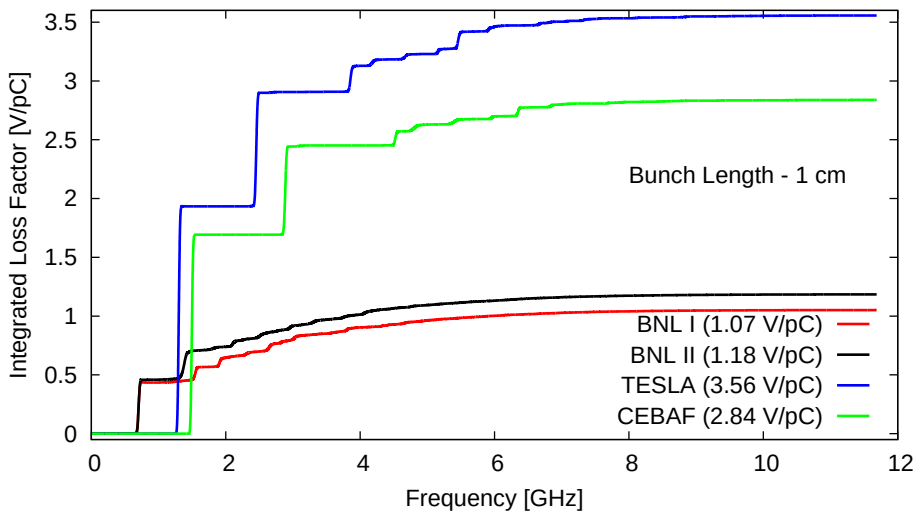

Figure 8.22: Integrated loss factor for BNL I geometry

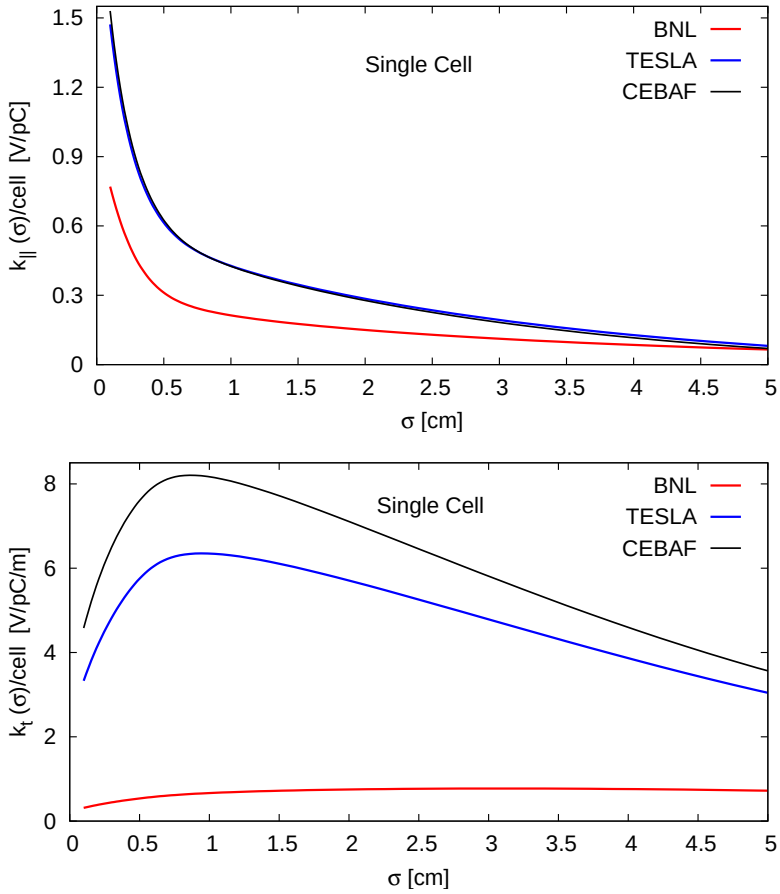

Figure 8.23: Logitudinal and transverse loss factors as a function of bunch length.

8.5 Multipass Multibunch Instabilities

In addition to the average HOM power, energy spread, and emittance growth, individual HOMs interacting with the beam beyond certain thresholds can cause instabilities. In SERLs, transverse multibunch beam breakup (BBU) is one of the main limiting factor primarily driven by high Q dipole modes. A bunch traveling through the cavity with an offset can excite a transverse HOM (mainly dipole) and the subsequent bunch will exprience a momentum kick

$$\delta p = \frac{q}{c} W(\tau) \tag{8.30}$$

where, $W(\tau) = \frac{cZ_\perp}{2Q} \sin(\omega\tau) e^{-\omega\tau/2Q}$.

The bunch returns back to the cavity on its recirculation path with the momentum kick translated to a transverse displacement through the M_{12} component of the recirculated matrix. If the bunch returns back "in-phase" with the HOM, it can form a closed feedback loop between the beam and cavity. If the Q_{ext} is sufficiently large, the induced voltage in the HOM grows exponentially and leads to beam breakup. An analytical expression was developed for a single dipole HOM with a single recirculation pass which is given by [97]

$$I_{thr} = \frac{-2p_r c}{e\left(\frac{R}{Q}\right) Q_e k_m M_{12} sin(\omega_m t_r)} \tag{8.31}$$

where p_r is the momentum of the recirculating beam, c is the speed of light, $Q_e \frac{R}{Q}$ is the impedance of the HOM, k_m is the wave number, M_{12} is the transport matrix of the recirculation path and t_r is the recirculation time.

Threshold current calculations for cavities with a train of bunches through N cavities, each with several HOMs are usually carried out with numerical methods. Several numerical codes have been developed to simulate multibunch BBU and estimate threshold currents for SRF cavities with high Q deflecting modes [91, 92, 93, 94]. Simulations can be performed in both time domain (for example TDBBU [91]) and frequency domain (for example MATBBU [92]). In time domain the transverse phase space of the bunches is calculated through each RF cycle and the cavity excitation levels is correspondingly updated. This procedure is iterated through several RF cycles either to reach a steady state or beam break up for given threshold current. In the frequency domain a steady state solution can be formulated into a system of linear equations. The eigenvalues for each coherent frequency can be computed which are simply the inverse of the complex currents. The values corresponding to the positive real axis are physically realizable currents which determine the threshold for that frequency. A sample computation of complex currents as the frequency is stepped through region of interests is seen in Fig 8.24. Both numerical techniques usually treat a cavity as a drift space with an accelerating gap and an impulse kick at the center of the cavity to represent the effect of the deflecting mode.

Simulations were performed for an electron cooling scenario shown in Fig. 6.3 with four cavities to accelerate the electron beam from 2 MeV to 54 MeV. A threshold current of 2 Amps show no growth of multibunch BBU with a unit recirculating tranfer matrix. Due to manufacturing errors the HOM frequencies exhibit a random spread for different cavities. The reasonable HOM frequency spread ($\delta f \sim Q_{ext} f_{HOM}$) reduces the effective Q_{ext} of the mode and as a result increases the threshold current. Fig. 8.25 shows a simulation for a threshold

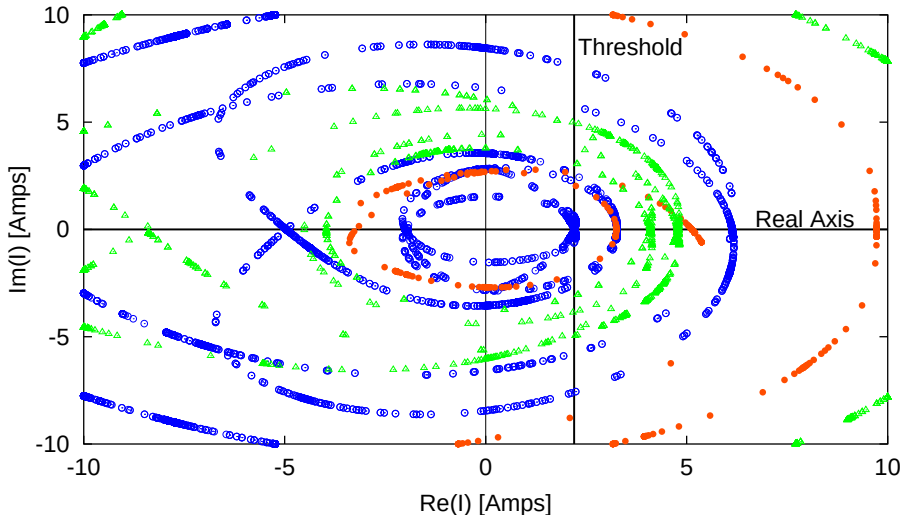

Figure 8.24: A computation of complex eigenvalues for each frequency sample from 0.8 to 1.8 GHz.

current of 2 Amps with different HOM frequency spread ranging from 3-10 MHz. A simulation using the same cavity and lattice parameters in MATBBU confirms the threshold current. Fig. 8.26 shows threshold current as a function of frequency and the limiting modes are mainly between 850-950 MHz and 1.7-1.8 GHz. This is consistent with the impedance measurements of the modes in these regions ($Q_{ext} \approx 10^4$). The case with no HOM spread shows a slightly smaller threshold current as expected and the simulations results are within the discrepancies expected between the two codes [98]. Since the threshold current is also dependent on M_{12}, lattice techniques such as reflection and rotation can be employed to further supress multibunch BBU in recirculating linacs [94].

8.6 Power Coupler Kick

The fundamental power coupler (FPC) is a co-axial antenna with a rounded tip placed on the 24 cm beam pipe as shown in Fig. 8.12. The design is adapted from an SNS FPC [101] due to the proximity of frequency (805 MHz). The average input power is approximately 25 kW which requires a Q_{ext} of approximately 3×10^7. Fig. 8.27 shows a plot of the Q_{ext} as a function of the penetration depth of the inner conductor of the coaxial line. The required Q_{ext} can be achieved without any penetration into the beam pipe. Note that the Q_{ext} was calculated using the 3 db bandwidth of the transmission coefficient

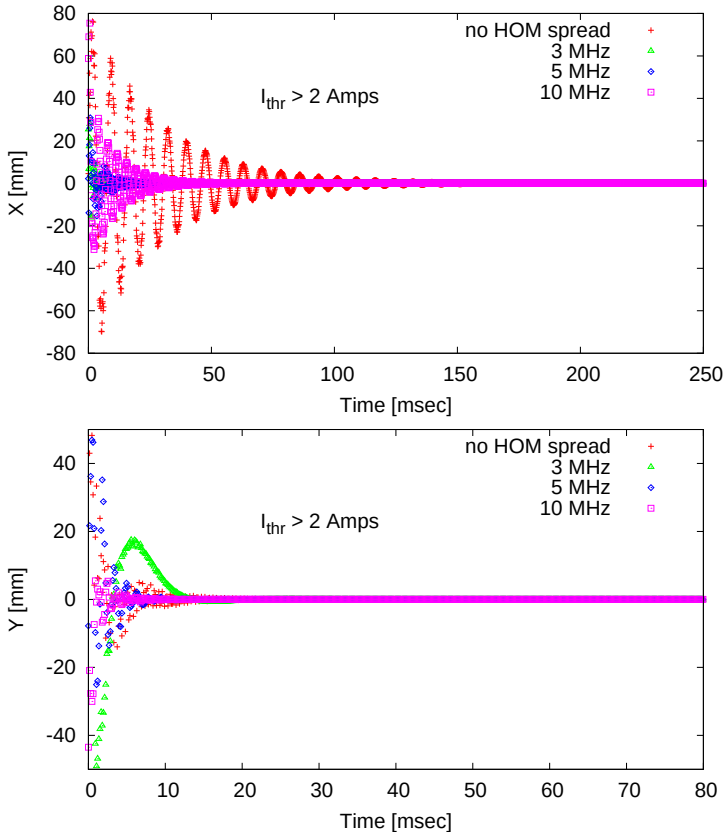

Figure 8.25: Time domain simulation using TDBBU for an electron cooling scenario with four five-cell cavities to accelerate the beam from 2 MeV to 54 MeV. The threshold current was set at 2 Amps with 40 dipole HOMs with both polarizations and show no growth of multibunch BBU for an arbitrary M_{12}.

S_{21} in the frequency domain of Microwave Studio [102].

The presence of single FPC can lead to a non-zero transverse field on-axis resulting in a kick to a bunch traversing the structure. The FPC is placed at the exit of the linac to alleviate the effect of the tranverse kick so that beam experiences the kick at a higher energy. In the absence of a symmetric coupler to cancel the effect, a symmetric stub can be placed to reduce the transverse kick. Also, the large beam pipe and relatively weak coupling are natural remedies to help minimize the transverse kick. The transverse fields for the case of a single coupler with and without a symmetrizing stub and a symmetric coupler with a 1 mm relative offset is shown in Fig. 9.22 and the respective transverse kicks are computed using a similar approach described

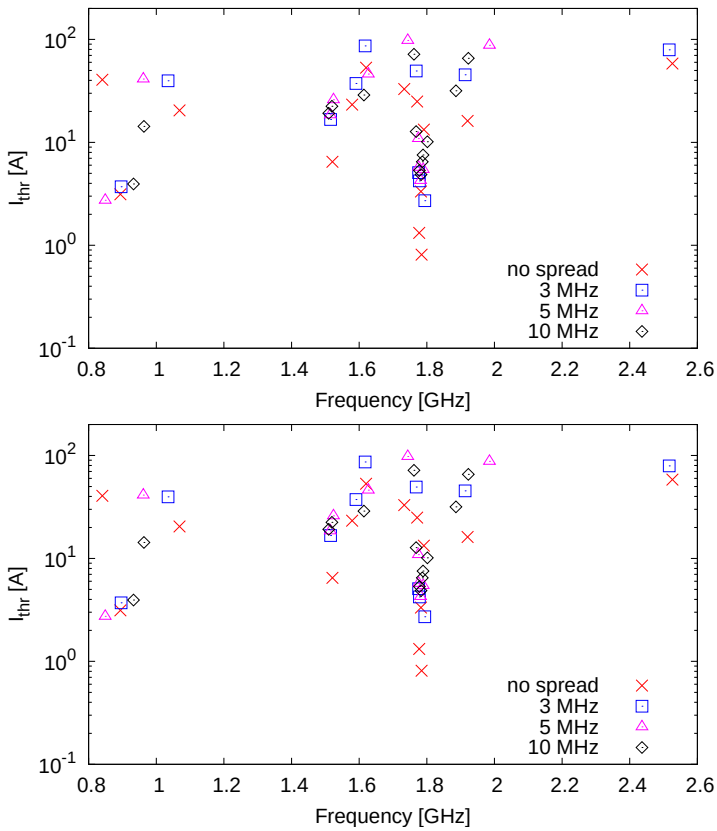

Figure 8.26: Frequency domain simulation using MATBBU for the same electron cooling scenario. The threshold current are above 2 Amps for three different frequency spreads. The limiting modes are mainly near two different regions (850-950 MHz and 1.7-1.8 GHz) as expected. 40 dipole HOMs with both polarizations were used in the simulation for an arbitrary M_{12}.

in [103, 104].

The transverse "kick factor" is simply given by

$$\delta_t = \frac{\int (E_y + cB_x)dz}{\int E_z dz} \tag{8.32}$$

which can be numerically evaluated. The kick received by the bunch passing through is dependent on the relative phase between bunch and the RF and is given by

$$\frac{p_t}{p} = \frac{eV_{acc}}{pc}\mathrm{Re}\left(\delta_t e^{i\phi_0}\right) \tag{8.33}$$

where ϕ_0 is the bunch phase with respect to the RF, and V_{acc} is the voltage

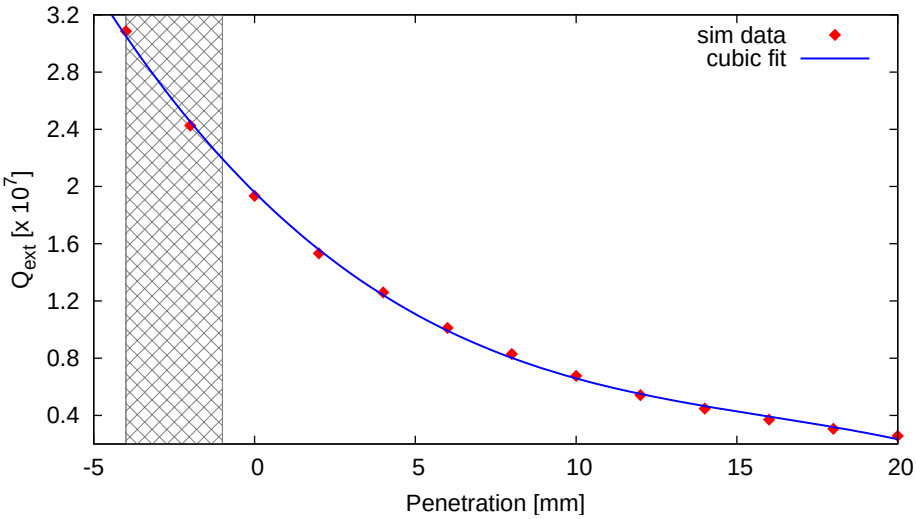

Figure 8.27: A scan of Q_{ext} as a function of the penetration of the tip into the beam pipe. The solid line is a quadratic fit to the calculated Q_{ext} points. The shaed region shows the expected penetration to achieve the required Q_{ext} of approximately 3×10^7.

of the accelerating gap. The normalized emittance growth due to the time dependent RF kick can be estimated using the formula derived in Ref. [105] which is given by

$$d\epsilon_n = \sigma_t \frac{2\pi\sigma_z}{\lambda_{RF}} \frac{eV_{acc}}{E_0} |\delta_t e^{\phi_0}| \tag{8.34}$$

where σ_t and σ_z are the transverse and longitudinal beam sizes, and E_0 is rest energy of the e^-. Table 9.5 shows the kick factors, transverse kicks, and the corresponding emittance growth for three cases with transverse RF fields. In all three cases, the kicks received are quite small and amount to negligible emittance growth compared to the growth induced by space charge.

Table 8.6: Transverse kick and normalized emittance growth for a single coupler,dual coupler with 1 mm asymmetry, and a single coupler with a symmetrizing stub, both with a $Q_{ext} \approx 3 \times 10^7$.

Scheme	$\delta_t \times 10^{-4}$	Kick
Single Coupler	(-9.3 + 1.2i)	0.85 mrad
Single Coupler + Stub	(3.0 - 3.8i)	0.27 mrad
Dual Couplers (offset)	(0.6 - 0.6i) mm^{-1}	50 μrad

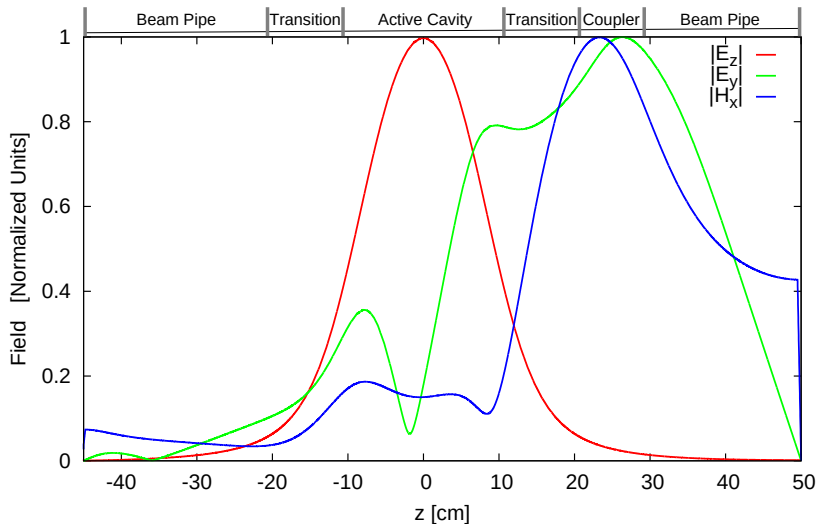

Figure 8.28: Longitudinal and transverse fields on-axis of the SRF cavity due to transverse coaxial coupler. The calculations were carried out using a single cell with the same transition sections as the five-cell cavity and normalized to 15 MV/m for the kick calculations.

8.7 Multipacting

Multipacting in RF structures is a resonant electron multiplication caused by secondary electrons emitted from the cavity surface. Primary electrons emitted from the surface impact back in an integer number of RF cycles causing emission of secondary electrons. If the secondary electron yield (SEY) of the surface is greater than 1, the resonant emission can lead to an avalanche, absorbing RF power and also lead to loss of superconducting properties locally, and sometimes result in thermal breakdown.

The Helsinki code, MultiPac 2.1 [99, 100], is used to calculate the field levels at which multipacting can be onset. Since the five-cell design is made of identical $\frac{1}{2}$ cells, it is sufficient to perform a simulation for single cell. Fig. 8.29 shows the counter function representing the total number of electrons (primary and secondary) and the corresponding impact energies as a function of peak surface field for BNL I and II designs. The total number of electrons after a given number of impacts normalized to the average secondary emission coefficient corresponding to the impact energy (enhanced counter function) is shown in Fig. 8.30 as a function of peak electric field.

An enhanced counter function (ECF) larger than 1 represents an onset of multipacting at that field level. Fig. 8.30 shows a region of interest at high

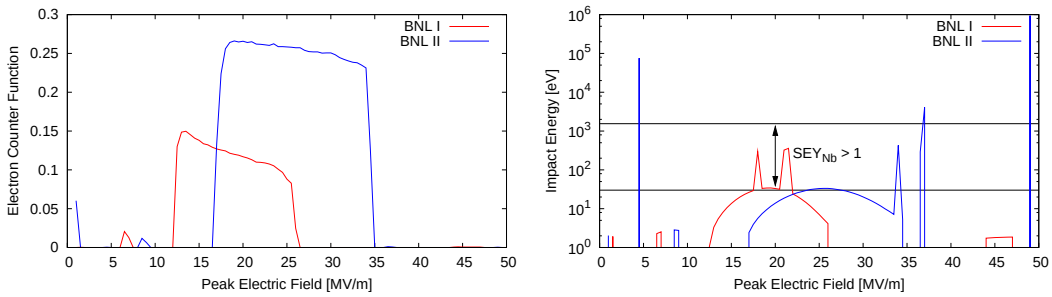

Figure 8.29: Top: The electron counter function representing the total number of free electrons after a given number of impacts (20) as a function of peak electric field. Bottom: The final impact energy of the electrons surviving the maximum number of impacts (20) as a function of peak electric field.

surface fields (15-40 MV/m). The impact energies between 15-40 MV/m are quite low (< 30 eV) and the the corresponding SEY for niobium is smaller than 1. Therefore, the ECF is much smaller than 1 therefore making multipacting very unlikely for both BNL I and II designs. It is interesting to note that peak of the ECF for BNL I is located at 20 MV/m which is approximately a factor of 2 smaller than expected surface field ($E_{peak} > 40$ MV/m). BNL II design has more peaks which are located closer to the operating surface fields.

The electron trajectory for BNL I (also similar to BNL II) near field region of ≈ 20 MV/m is shown in Fig. 9.6 which exhibits stable two point multipacting.

8.8 Lorentz Force Detuning

The surface fields on the cavity exerts a force on the walls which are non-negligible at high gradients. The radiation pressure due to Lorentz force is given by

$$P_{rad} = \frac{1}{4}\left[\mu_0|\vec{H}|^2 - \epsilon_0|\vec{E}|^2\right] \tag{8.35}$$

where $\vec{H}$ and $\vec{E}$ are the magnetic and electric fields on the surface. Fig. 8.32 shows a plot of the surface fields and radiation pressure for BNL I.

The radiation pressure deforms the cavity and results in a frequency shift which is expressed as

$$\delta f \propto \frac{f_0}{4U}\int_{\delta V}\left(\epsilon_0|\vec{E}|^2 - \mu_0|\vec{H}|^2\right) dV \tag{8.36}$$

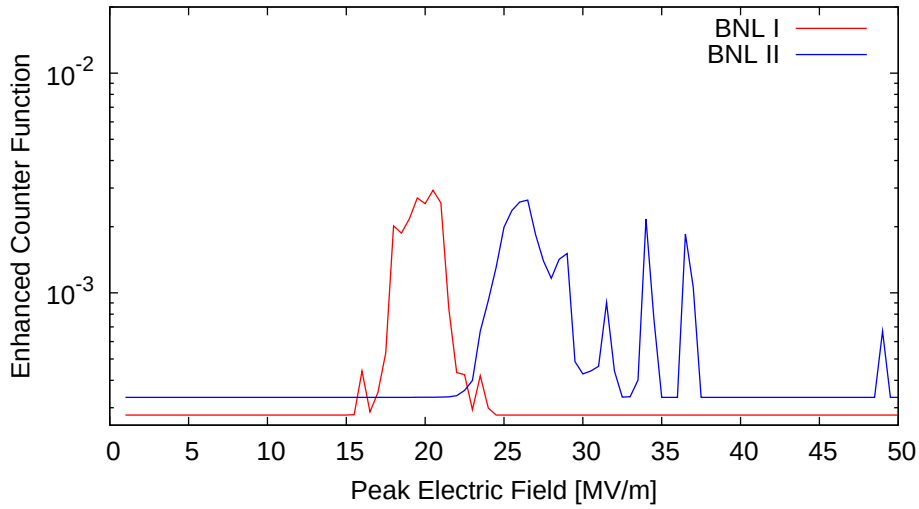

Figure 8.30: The enhanced counter function which represents the number of secondary electrons after a given number of impacts normalized to the secondary emission coefficient corresponding to the impact energies plotted as a function of peak electric field.

where f_0 is the resonant frequency, U is the stored energy, and δV is the fractional change in volume. Assuming that change in volume is small compared to the cavity and scales linearly with pressure, the static frequency shift for a given E_{acc} is given by

$$\delta f = -K_L E_{acc}^2 \tag{8.37}$$

where, K_L is the Lorentz detuning coefficient which is a figure of merit of the stiffness. Fig. 8.33 shows the effect of radiation pressure on the cavity shape for an $E_{acc} = 1$ MV/m with a wall thickness of 3 mm. The Youngs modulus and the Poisson's ratio were taken to be 103 GPa and 0.38 respectively.

Due to the high Q (3×10^7) operation, a small coeffecient is necessary. K_L for the BNL I cavity was calculated to be 1.28 Hz/(MV/m)^2 and is compared to the stiffened TESLA and CEBAF cavities in table 8.5. An independent calculation carried by AES [107] determined K_L to be 1.2 Hz/(MV/m)^2. Due to inherent stiffness of the cavity shape, no special stiffening rings are required. The simulations were performed using ANSYS [108] with fixed ends on both sides. The tuner end of the cavity is not absolutely fixed which may result in slightly larger K_L.

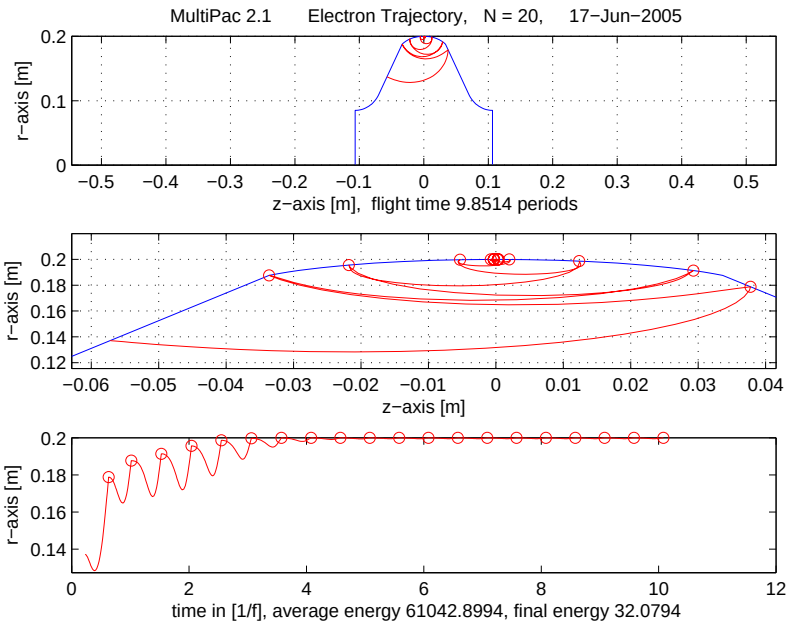

Figure 8.31: Electron trajectory calculated for a peak field of approximately 20 MV/m which shows a stable two point trajectory but no multipacting is expected due to impact energies smaller than 30 eV.

8.9 Conclusion

A five-cell SRF linac cavity has been designed to operate at 703.75 MHz to accelerate ampere class beams in an energy-recovery mode. The design is optimized to propagate the large HOM power through the beam pipe to an external ferrite load operating at room temperature. Several aspects of the cavity design and HOM characteristics have been simulated and benchmarked with measurements on a copper prototype. Extensive comparisons have also been made to the other existing SRF cavities being proposed for SC-ERLs. Multipass multibunch simulations have been carried out and the threshold currents for the onset of the instabilty is set at ~ 2 Amps. Issues relating to fundamental power coupling, transverse kicks, multipacting, bellows shielding, and Lorentz force detuning have also been addressed.

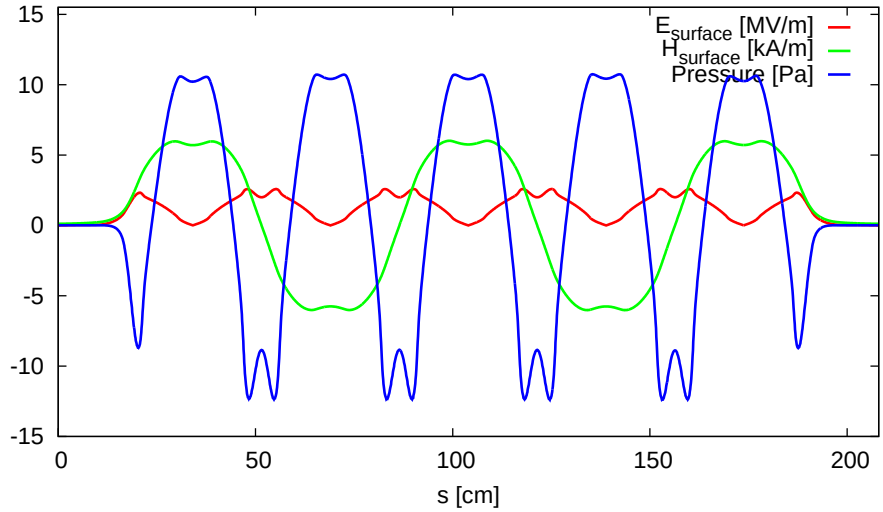

Figure 8.32: Electric and magnetic fields on the surface of the five-cell BNL I design and the corresponding radiation pressure as a function of longitudinal position.

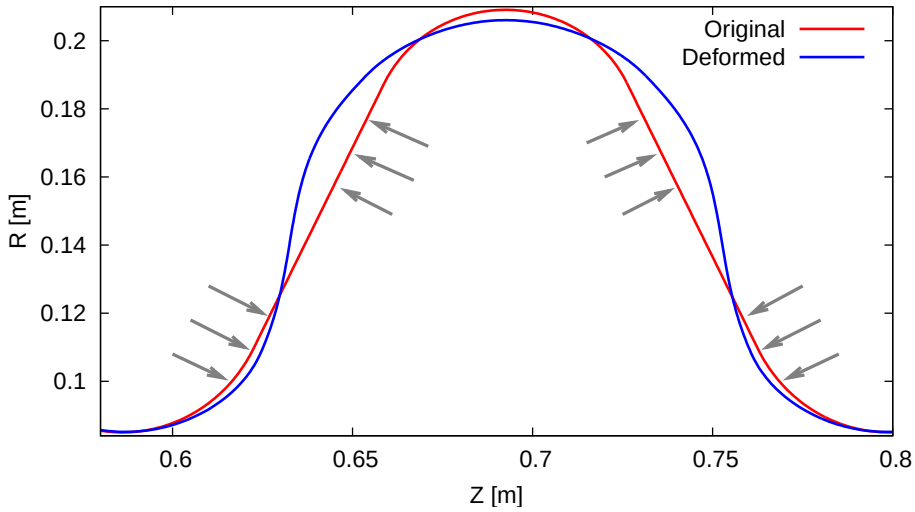

Figure 8.33: Deformation of the cavity walls due to Lorentz forces. The surface magentic field at the equator pushes the walls outward and surface electric fields at the iris pushes the walls inward. The deformation has been magnified to illustrate the effect.